Review scientific paper

Informacije MIDEM
Journal of Microelectronics,
Electronic Components and Materials
Vol. 44, No. 2 (2014), 87 – 103

Evaluation and analysis of methods for fixed and variable MEMS inductors design

Fatemeh Banitorfian[1], Farshad Eshghabadi[1], Asrulnizam Abd Manaf[1], Patrick Pons[2], Norlaili Mohd Noh[1], Mohd Tafir Mustaffa[1], Othman Sidek[1]

[1]Advanced Integrated System Device Group (AISDe), School of Electrical and Electronic Engineering, Universiti Sains Malaysia, Engineering Campus, Nibong Tebal, Malaysia
[2]CNRS, LAAS, Toulouse, France

Abstract: This paper investigates fixed and tunable MEMS inductors. A detailed technical discussion is given on those parameters that influence the inductance, quality factor, resonance frequency, and tuning range. Based on these parameters, the available methods are reviewed and categorized for both fixed and tunable inductors to improve the quality factor and tuning range. The major research issues in fixed MEMS inductors are the quality factor and the resonant frequency. The tuning range, in addition to the quality factor, is the main research issue of tunable MEMS inductors. Several comparison graphs are given to show the performance of each method. The parameters and their effect on the performance of the inductor were analyzed and simulated by MATLAB to present their pros and cons, their effectiveness, and their failures. This exploration can assist the designers to choose the appropriate methods for developing fixed and tunable inductors in terms with their desired application and specification. In this technical review paper, a detailed comparison between the inductors parameters for different techniques of development and adjustment gives the researchers a deep understanding of available solutions.

Keywords: Passive circuits, Inductors, Q factor, Simulation, Microelectromechanical devices

Evaluacija in analiza metod za oblikovanje fiksnih in variabilnih MEMS tuljav

Izvleček: Članek raziskuje fiksne in nastavljive MEMS tuljave. Podana je natančna tehnična razlaga parametrov, ki vplivajo na induktivnost, faktor kvalitete, resonančno frekvenco in območje nastavljanja. Na osnovi teh parametrov so predstavljene in kategorizirane obstoječe metode povečanja faktorja kvalitete in območja nastavljanja za fiksne in nastavljive tuljave. Glavni raziskovalna izziva pri fiksnih MEMS tuljavah sta faktor kvalitete in resonančna frekvenca. Območje nastavljanja je poleg faktorja kvalitete najpomembnejši raziskovalni faktor pri nastavljivih tuljavah. Podani so številni grafi, ki prikazujejo prednosti vsake metode. Z namenom prikazovanja prednosti in slabosti ter učinkovitosti metod so bili parametri in njihovi vplivi na delovanje tuljave analizirani in simulirani s simulatorjem Matlab. Ta raziskava lahko pomaga načrtovalcem pri razvoju fiksnih in nastavljivih tuljav. V tem preglednem članku obsežna primerjava parametrov tuljav razvitih z različnimi tehnikami podaja raziskovalcem razumljiv in celosten vpogled v delovanje in razumevanje obstoječih rešitev.

Ključne besede: pasivna vezja, tuljave, Q faktor, Simulacije, MEMS strukture

** Corresponding Author's e-mail: banitorfian.f@gmail.com*

1 Introduction

Recently, rapidly increasing interest for small-sized high-performance wireless systems has led to a high demand for integrated passive devices in radio-frequency integrated circuit (RFIC) applications. Inductors play a key role in radio frequency (RF) circuits. Conventional on-chip inductors are spiral inductors that are utilized in portable wireless communication circuits to meet the desired system specifications, such as: low cost, low voltage supply, small size, low power dissipation, low noise, high frequency of operation, and low distortion [1, 2]. The most important applications for inductors are in: impedance matching networks, a voltage controlled oscillator (VCO), LC tanks in a VCO, multi-band RF filters, multi-band monolithic microwave integrated circuitry (MMIC), power amplifiers in radio transmitters,

low-noise amplifiers (LNAs), and double-balanced Gilbert-cell mixers [3-6].

Currently, there are several drawbacks that limit the performance when employing conventional planar MMIC inductors, such as substrate parasitics and the conductivity of silicon substrate [2], which cause low resonance frequency and low *Q* factor [6-8]. The best approach to reduce the effect of substrate conductivity is to use MEMS technology with which high *Q* and high performance can be achieved [2, 9]. The MEMS inductor gives a very high *Q* factor compared with the MMIC inductor. This can improve sufficiently the noise figure in LNAs and the phase noise in VCOs. Also, the MEMS inductor can be implemented to be tunable, whereas the MMIC inductor cannot.

The most important parameter in fixed MEMS inductors is the quality factor, which can be improved by several techniques. These methods can be listed briefly as: substrate effects reduction by removing the substrate under the coil or increasing the distance between the substrate and the metal coil, in order to reduce the capacitive and inductive coupling [8, 10, 11] or decoupling (such as vertical planar inductor) [12, 13]; the use of 3D inductors to reduce losses inserted by the eddy current that is generated in the substrate [14]; the use of a patterned-ground layer between the spiral and substrate [15]; the use of high resistivity substrate [16]; the use of high conductivity metal for inductors [17, 18]; and changes to the thickness and width of the metal [19].

In tunable MEMS inductors, in addition to the *Q* factor, the tuning ratio is a research issue. Briefly, the methods to improve the tuning range are: change the number of turns [9, 20], change of coupling capacitance [21-24], switched inductor [5, 25], change of mutual inductance (in transformer type) [3, 4, 26, 27], change of the permeability [28-31], and counteractive magnetic field induction [32, 33].

In this paper, the advantages and disadvantages of each method are considered and a detailed comparison and analysis among these methods is presented. Section II discusses around the MEMS inductors' geometry, equivalent model and corresponding equations for inductance and quality factor. A detailed discussion for fixed-tuned MEMS inductor with available methods of quality factor enhancement and their relative analysis is given in section III. In section IV, available methods to implement a tunable MEMS inductor and tuning range increase are described with the corresponding detailed analysis. Finally, the conclusion is given in section V.

2 MEMS Inductors

The growing market of the wireless and communication industry has caused a remarkable demand for integrated passive elements. Conventional MMIC inductors do not provide sufficient quality factor or the capability of tuning. However, MEMS inductors are suitable for replacing conventional MMIC inductors. The conventional form of on-chip inductor is spiral. There are different possible shapes for the fabrication of inductors such as square, hexagonal, octagonal and circular. The effect of these shapes on inductance was investigated in [34]. The circular type shows the best *Q* factor; because in the square type, the current distribution is crowded into the edge of the corners, such that the effective series resistance is increased. MEMS inductors are designed depending on application; integrated MEMS inductors on Si wafer appear to be very interesting for future RF and microwave functions and communication systems. Currently, the most demanded application for MEMS inductors is in reconfigurable wireless systems such as satellite communication and mobile handsets [35]. The general model showing planar inductor performance is illustrated in Figure 1. L_s indicates the low-frequency inductance and R_s gives the series resistance of the coil. The capacitance between the different windings of the inductor is shown by C_s, including the air core as the covering dielectric layers. C_{ox} is the oxide (or polyamide) capacitance layer between the windings and the silicon (or GaAs) substrate, C_{Si} is the capacitance between the coil and the ground through the silicon substrate, and R_{Si} is the eddy current losses in the substrate [36].

Considering the inductor model in Figure 2, the quality factor *Q* of the inductor is given by [10]:

$$Q = \frac{\omega L_s}{R_s} \times \frac{R_p}{R_p + R_s\left[\left(\frac{\omega L_s}{R_s}\right)^2 + 1\right]} \times \left[1 - \frac{R_s^2\left(C_s + C_p\right)}{L_s} - \omega^2 L_s\left(C_s + C_p\right)\right] \tag{1}$$

$$Q = \frac{\omega L_s}{R_s}\left(\text{substrate loss}\right).\left(\text{self resonance loss}\right) \tag{2}$$

$$R_p = \frac{1}{\omega^2 C_{ox} R_{si}} + \frac{R_{si}\left(C_{ox} + C_{si}\right)^2}{C_{ox}^2} \tag{3}$$

$$C_p = C_{ox} \times \frac{1 + \omega^2\left(C_{ox} + C_{si}\right) C_{si} R_{si}^2}{1 + \omega^2\left(C_{ox} + C_{si}\right)^2 R_{si}^2} \tag{4}$$

$$R_s = \frac{\rho}{\delta w} \tag{5}$$

$$\delta = \sqrt{\frac{\rho}{\pi \mu f}} \tag{6}$$

where R_s is the resistance per unit length (R_s) and ρ is the metal resistivity in Ω-cm, W is the width of the inductor line, δ is the skin depth, $\mu = 4\pi \times 10^{-7}$ and is the free space permeability, and f is the operating frequency.

Equation (1) is used to calculate the Q factor for the pie model shown in Figure 1. This equation can be divided into three terms: the first term is the simplified equation for Q while all parasitics are neglected. In this term, the Q factor is found from the frequency inductance and series resistance. Hence, the only effective parameter in this term is series resistance, which depends on the metallization. The second and third terms are the substrate loss factor and self-resonance loss factor. For an ideal inductor, these two terms show a value of unity because no parasitic are considered.

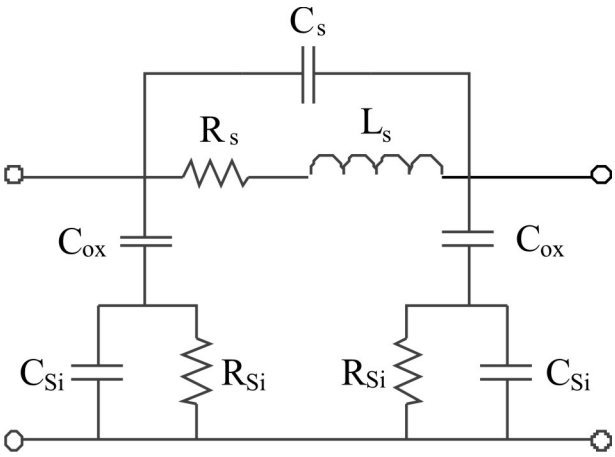

(*a*)

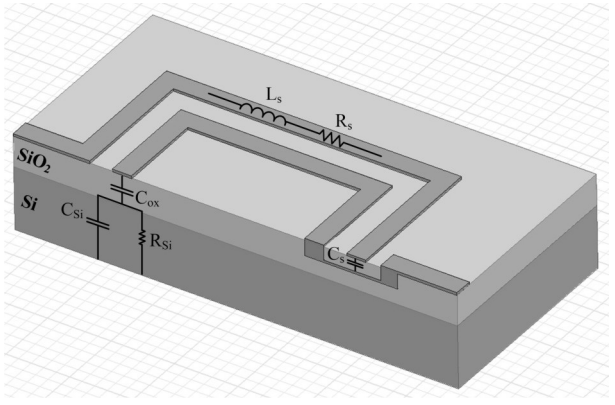

(*b*)

Figure 1: General model for planar spiral inductor (*a*) schematic view, and (*b*) perspective view.

According to (1) and (4), the metallization thickness W and the parasitic capacitance C_p are two effective parameters in the Q factor equation. This means that an increase in Q is directly achieved by reducing the series resistance. Using (5), it can be seen that R_s is directly proportional to $\sqrt{f}$ and that reactance is proportional to f (equation 9). Thus, Q is also approximately proportional to $\sqrt{f}$ [36]. Therefore, this parameter is usually more effective when the frequency is low enough. There are several methods to enhance the Q factor using metallization, which will be described in the next section.

In addition to the Q, the parasitic capacitance affects the resonance frequency; the resonance frequency can be achieved by:

$$f_r = \frac{1}{2\pi\sqrt{L_s(C_s + C_p)}} \tag{7}$$

From (7), it can be observed that series resistance has no influence on resonance frequency. The inductor impedance Z_L and corresponding quality factor Q, is achieved by:

$$Z_L = R_s + j\omega L \tag{8}$$

$$Q = \frac{L\omega}{R_s} \tag{9}$$

A reduction in the parasitic capacitance not only pushes the resonant frequency higher (equation 7), but also results in a large reactance (equation 8), and therefore, a high Q inductor (equation 9) at high frequencies.

In a tunable MEMS inductor, in addition to the quality factor, the tuning inductance range is another important parameter. The inductance value depending on the shape of the inductor is calculated using different equations. Most previous works discuss the square shape due to its easy fabrication, but the best results are achieved for a circular spiral inductor. For a single-layer spiral inductor, regardless of its layout shape (square, hexagonal, octagonal, and circular form), a generalized equation for inductance is [37]:

$$L = \left[\frac{\mu_0 N^2 D_{AVG} C_1}{2}\right]\left[\ln\left(C_2/\rho\right) + C_3\rho + C_4\rho^2\right] \tag{10}$$

where N represents the number of turns; μ_0 is the vacuum permeability and is equal to $4\pi x10^{-7}$; ρ is the fill ratio; D_{AVG} shows the average diameter; D_{in} and D_{out} are the inner and outer diameter, respectively, and can be found from Figure 1. C_1–C_4 are the coefficients depending on the layout and their values can be found from [37], depending on whether the inductor is a square, hexagonal, octagonal, or circular type.

Generally, the main parameters in an inductor are: the Q factor, the inductance value (L), the resonance frequency, and the size. Each of these parameters is dependent on some other factors such as metallization

and parasitic capacitances. According to these relations, several methods to enhance the *Q* factor and the tuning range were presented. In the following sections, most of these methods will be discussed.

3 Fixed MEMS inductors and methods to enhance the quality factor

The main research issue for fixed-value MEMS inductor is the quality factor. According to (1) and the discussion in section II, previous works have employed several methods improve the *Q* factor. Here, based on equation (2), the quality factor enhancement methods were divided into three categories: series resistance reduction, substrate loss reduction, and self-resonance loss.

3.1 Series Resistance Reduction

The first term of equation (1) shows that the only effective parameter in this term for improving the *Q* factor is series resistance (R_s). Equation 5 shows that (R_s) is dependent on other parameters, such as: metal resistivity, length, skin depth, and effective area. The effects of these parameters and the relevant previous works were studied.

3.1.1 The Skin Effect Reduction

Applying a time-varying voltage to the spiral inductor, a magnetic field arises from the time-variant current. This causes a current induction in the substrate and tracks. The induced eddy current in the substrate causes the substrate loss. By increasing the frequency from lower frequency to higher frequencies, the domination of a dc current density and its corresponding magnitude of fields exponentially decrease, while the opposing penetrated electric field increases due to the growing eddy current. This is called the skin effect, which cancels the current flows at the center of the conductor and forces it to flow in the outer area (skin). This reduces the effective sectional area of the conductive metal, which results in frequency-dependent growth in the series resistance R_s. The increase rate can be found by the skin depth, which is the effective depth of penetration (δ) of the current [38] and its equation is given in (6). In addition, the flux coupling reduction causes the decrease in the self-inductance value at higher frequencies. The series resistance R_s in (5) can be found with (5), which neglects the skin effect induced by the substrate, but not the skin effect induced by the coil segments. For frequencies of 2 GHz and below, the skin effect is negligible; whereas for frequencies above 2 GHz, the inverse-frequency-dependent skin depth is much less than the conductor's width.

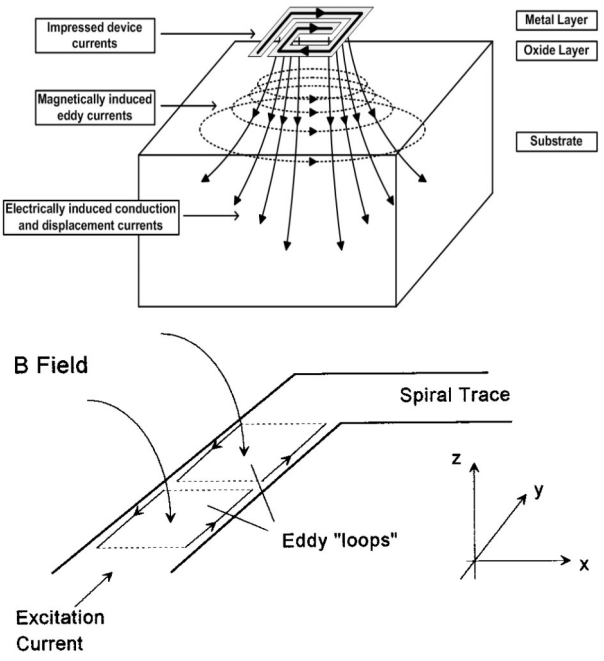

Figure 2: Eddy and displacement current in the substrate induced by the current flow in spiral inductor [39] (top), and self-induced current by skin effect [40] (bottom).

Two spiral inductor circuit models considering the skin effect induced by the substrate were developed by [40] and [41], which are more intuitive and accurate. The estimation of the effective series resistance $R_{s,\text{eff}}$ was given by [40] as:

$$R_{s,\text{eff}} = R_{\text{DC}}\left[1+\frac{1}{10}\left(\frac{\omega}{\omega_{\text{crit}}}\right)^2\right] \tag{11}$$

where R_{DC} is the dc series resistance of the coil and ω_{crit} is the frequency at which the current crowding begins to become significant.

Based on [40], this model was modified by [41] and the following equation for substrate-induced series resistance was developed as:

$$R_{s,\text{eff}} = R_{\text{DC}}\left[1+\frac{\omega^2\left(0.035W^4T^2\sigma^2\mu_0^2\right)}{P^2}\sum_n\left(\frac{n-M}{N-M}\right)^2\right] \tag{12}$$

Figure 2 shows the currents induced by the skin effect and the substrate into the planar inductor. Using the available models based on equations (5), (11), and (12), the quality factor of a spiral inductor was plotted in Figure 3 to compare the calculated *Q*s versus frequency. The top plot in Figure 3 is based on calculated R_S with (5), in which induced skin effect by the substrate is ne-

glected. *N* increase in *Q* can be observed in the given frequency range; however, the *Q* slope shows a decrease because of the induced skin effect by its own segments. The middle and bottom plots show the calculated *Q* from (11) and (12), which show a decrease in *Q* as the frequency increases. This means that the induced skin effect by the substrate cannot be neglected after a determined frequency.

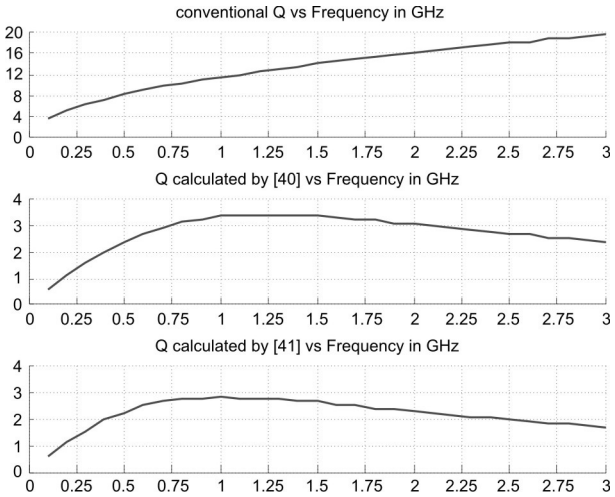

Figure 3: Calculated Q based on self-induced skin effect and substrate-induced skin effect.

Recently, stressed-metal high-*Q* 3-D inductors have been introduced. Dissimilar to the spiral inductors, the magnetic field in these inductors is not perpendicular to the substrate, which causes a reduction of losses associated with eddy currents generated in the Si substrate; thus, very high quality factors up to 1 GHz frequency were achieved. At higher frequencies, the magnetic field penetration into the lossy Si substrate causes a significant decrease of the quality factor. Employing a stressed-metal technology, silicon-based high-*Q* 3-D inductors were fabricated by [14]. The existence of low-k dielectric (SU-STM) materials under the inductors showed the increase in the self-resonance frequency. The simplicity and full compatibility with silicon and compound-semiconductor technologies are the two main advantages of this technique. This also allows the post-processing implementation. In [8], the *Q* factor was controlled with eddy current reduction. Here, the angular distance of the coil θ was displaced from 0 degrees to 90 degrees, as shown in Figure 4. This led to fewer magnetic flux lines, associated with the excitation current, penetrating through the silicon substrate. This results in a decrease of the skin effect and hence, the inductive loss and then quality factor can be tuned. In this work, using the decoupling effect, the *Q* factor was controlled between 2.9–5.2 at 2 GHz with an inductance variation between 8–16 nH.

When θ is 90 degrees, the maximum value for the *Q* factor is achieved because the substrate effect on the skin depth is a minimum; therefore, the inductor displacement can be categorized as two categories of coupling reduction ($\theta < 90^o$) and de-coupling ($\theta = 90^o$). The increase of the distance is an approach for coupling reduction. To achieve the de-coupling, the inductor is displaced in the vertical position, such as in [12]. This approach was based on a fully parallel batch process. Another vertical inductor fabricated by [13] shows the improvement in *Q* factor; in this work, plastic deformation magnetic assembly (PDMA) technology was employed to implement the inductor vertically (see Figure 5).

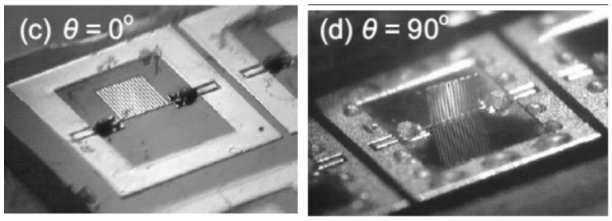

Figure 4: *Q*-controlled spiral inductor by variable angular distance [8].

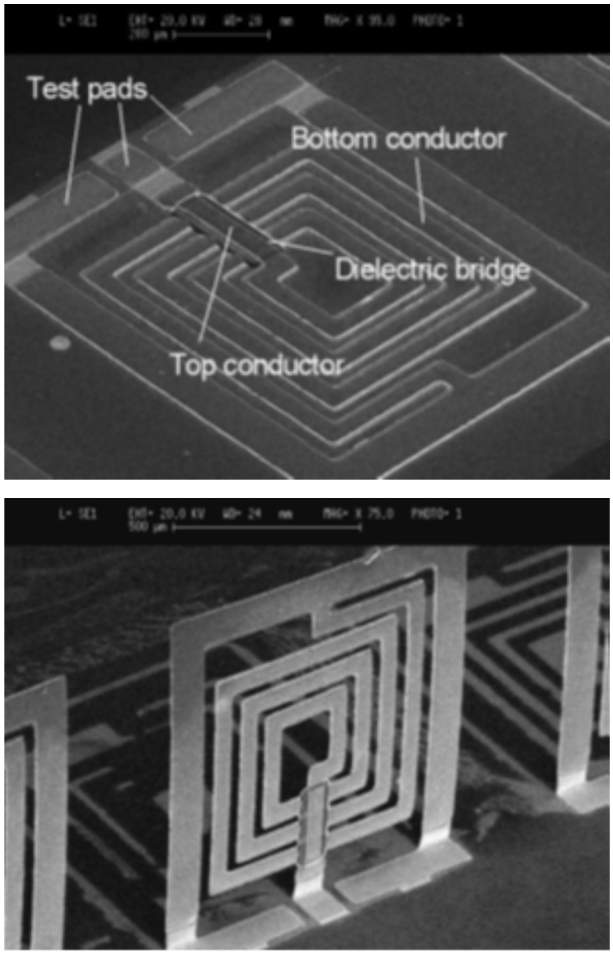

Figure 5: PDMA vertical spiral inductor [13].

When the inductor lies on the substrate without any distance, a *Q* factor of 3.5 is achieved at 1 GHz; this is the minimum value for the Q of this inductor. However, in the vertical position, the *Q* factor is 12 at the same frequency.

The approaches in [12] and [13] can be analyzed for their extensive separation between coil and substrate (a few hundreds of μm); in this case, it is possible to analyze these approaches in the suspended inductor technique in the substrate loss reduction section.

3.1.2 High Conductivity Metal

According to equations (1) and (5), the metal resistivity influences the *Q* factor. Figure 6 presents the calculated *Q* while various metals are employed for implementation of the coil segments. Here, copper shows the highest conductivity compared with gold, and aluminum shows the highest *Q* factor because $\omega L/R_s$ increases with a decrease in series resistance R_s.

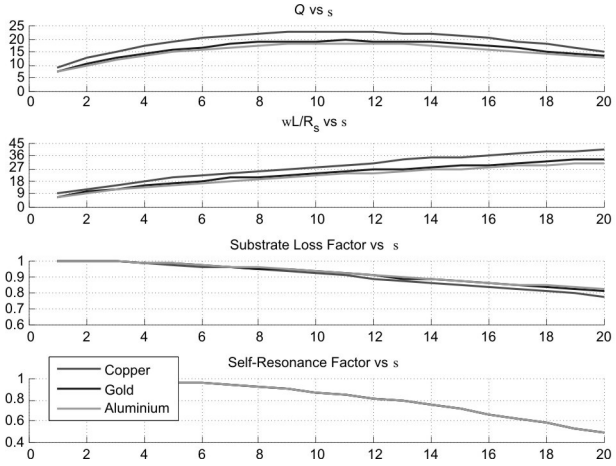

Figure 6: Calculated Q based on different conductive coil metals

Using high conductivity metal such as copper in the inductor is the most common technique to reduce metal loss in the inductor [42]. In addition to the material, the limited metallization thickness is one of the parameters that strongly influences the RF performance [17].

3.1.3 Width and Length Optimization

In addition to the conductivity of metal, the thickness and the width of the metal are also effective parameters to improve the *Q* factor because they influence the series resistance of the coil. Figure 7 shows the quality factor while the ratio of L/W sweeps from 50 to 450. The term $\omega L/R_s$ increases with a decrease of the L/W ratio; however, any increase in the L/W ratio causes an increase in the substrate loss factor and the self-resonance factor. It can be observed that the quality factor follows the behavior of the term $\omega L/R_s$ because it is more dominant than the other two factors in this specific case.

An optimum width and *Q* ratio was studied by [19]. In this work, a 3D inductor with different widths of metal was fabricated and measured. It was shown that the increasing width leads to an increasing quality factor while the resonance frequency remains constant. A comparison of the *Q* factor between several fabricated inductors was presented in terms of the change of their turn and width (see Table 1).

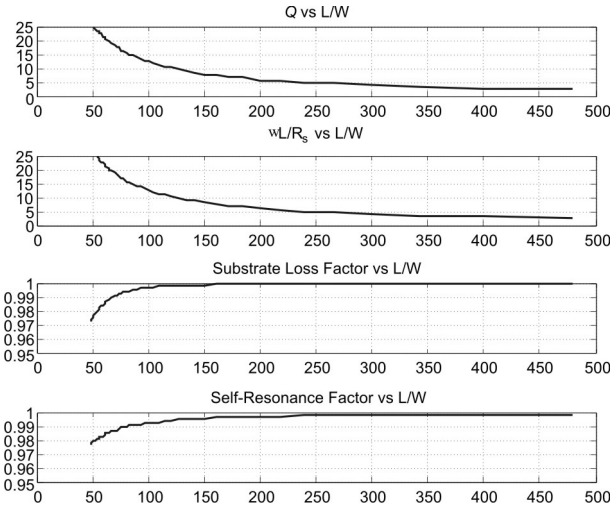

Figure 7: Calculated Q versus swept L/W ratio

Table 1: A comparison of q factor between fabricated inductors with different l/w ratio by [19]

Number of turns	Width (μm)	L (nH)	Quality factor	SRF (GHz)
1	25	1.23	38.2@7GHz	>40
1	35	1.22	51.6@7.5GHz	>40
1	45	1.16	137.5@12GHz	>40
2	25	2.60	30.5@3GHz	33
2	35	2.45	32.8@3.5GHz	35
2	45	2.20	66.1@7.5GHz	38

It should be noted that this method has some disadvantages, which should be considered in the calculation and design. Increasing the width causes an increase in the capacitive coupling; this might result in an undesirable performance of *Q*. [43] has mentioned this problem based on results of two identically fabricated inductors with different widths. The inductors were fabricated on silicon with a silicon oxide substrate. The metal used was copper, the number of turns was two, and the space between the two metals was 10 μm. The achieved *Q* factor for the inductor with a width of 80

μm was 10; however, the Q factor for the other inductor with a width of 50 μm was 17 at the same frequency of 1 GHz.

3.2 The Substrate Loss Reduction

According to equation (1), when the term for substrate loss factor is unity, the maximum quality factor can be achieved. To approach the unity value for the substrate loss factor, it is required that R_p be a very large value ($R_p \to \infty$) Equation (2) shows that when R_{Si} is equal to zero or infinity, R_p will limited to infinity. In addition, $C_{ox} = 0$ can cause an infinite-value of R_p. Based on this knowledge, to increase the value for R_p, four methods are conventional: (a) using high resistivity silicon [16], (b) etching away the silicon substrate [10, 19], (c) patterned grounded shields [15], and (d) increase the distance between the substrate and metal by suspending the coil [11]. The first two methods are usually used to realize $R_{Si} = \infty$, the third method is used to realize $R_{Si} = 0$, and the final method is used to realize $C_{ox} = 0$.

Figure 8 presents the effects of methods (a) to (c) on the quality factor. As can be observed, the high-resistivity substrate and patterned-grounded shields improve the quality factor compared with the conventional low-resistivity silicon substrate without any shields.

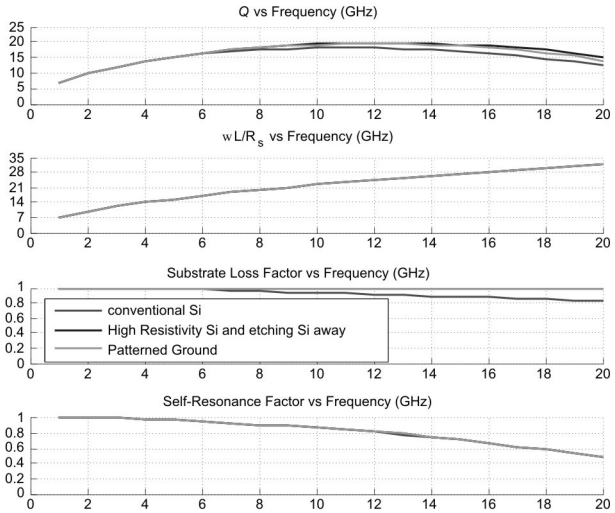

Figure 8: The calculated *Q* for different methods of substrate loss reduction

3.2.1 High-Resistivity Substrate

Increasing the substrate resistivity has the greatest effect on the second term in (1). As much of the substrate resistivity approaches infinity, it causes this term to approach unity. A low-resistivity substrate results in an inductor with high loss and therefore, low quality factor. In addition, the self-resonant frequency is very low because the Si substrate with its high dielectric constant introduces increased parasitic capacitances [16]. The resistivity of substrate R_{Si} is dependent on the employed substrate material. The substrate can be chosen from materials such as SiO_2/Si, high-resistivity silicon (HRS), glass, and quartz, the resistivity of each is increasing, respectively [38]. To obtain high-performance inductors, many approaches using: highly-resistive silicon with micro-machining technique [4], a glass layer [5], a thick polyimide layer [6], and a multilevel interconnection in the silicon substrate [7]–[9] have been reported, but their results are much lower than in [44].

In [44], a thick lower-cost and lower-process-time oxidized porous silicon (OPS) layer on s silicon substrate to fabricate a high-performance planar inductor was proposed. As a replacement for direct oxidation of bulk silicon, the short-time oxidation process of porous silicon was employed to make the oxide layer thicker than 30 μm by the reaction of the side wall of pores. This thick oxide layer prevents any harmful effects on the performance of the fabricated inductor because of the silicon.

In [45], to reduce the undesired effects of silicon, SOS (silicon on sapphire) technology was employed, which is from the SOI (silicon on insulator) family of CMOS technologies. In this approach, a hetero-epitaxial process for integrated circuit manufacturing that consists of a thin layer (typically thinner than 0.6 micrometers) of silicon was grown on a sapphire (Al_2O_3) wafer. As conventional models are less accurate for inductors created in newer RF-compatible processes with very high resistivity bulk material such as SOS, appropriate modeling for this approach was carried out by [45]. In this work, the simple four- and five-element frequency independent models with small-to-moderate sized (< 300 um) inductors to be fabricated in SOS and a six-element model for larger, high-*Q* spirals (e.g., 600 μm) were introduced. They accurately model the increase in resistance versus frequency from current crowding. The models show that substrate loss is reduced to negligible values relative to trace resistance loss.

A new inductive coupled plasma (ICP) etcher was employed by [17], dedicated to dielectrics anisotropic deep dry etching in order to discover a new method based on patterning the inductor directly in a quartz substrate. The major benefit of this method is the high resistivity of the quartz (2×10^{14} Ωcm at 20 °C), which greatly decreases the substrate-induced RF losses.

3.2.2 Etching Substrate Away

Etching a cavity underneath the inductor is another approach to meet $R_{Si} \to \infty$ and hence, $R_p \to \infty$. This technique greatly improves the quality factor. [43] used a

dry etching technique to remove the seed layer while it is perfectly contacted to the pillars. This approach produced a great improvement with a peak *Q*-factor of 17 at a frequency of 1 GHz. The inductance is about 3.2 nH in the frequency range between 50 MHz and 3 GHz while the resonance frequency is about 6 GHz.

Sheng-Hsiang Tseng proposed a fully CMOS-compatible MEMS inductor in TSMC 0.18-μm 1P6M CMOS process and also Chip Implementation Center (CIC) micromachining post process to remove the oxide between the coil metals and the silicon substrate under the inductor by utilizing dry reactive ion etching (RIE). In this work, a 1.88-nH micro machined inductor with a *Q* factor of over 15 was achieved at 8.5 GHz, and the improvement is up to 88% in maximum quality factor [46].

In [10], the Silicon substrate of an MMIC inductor in 0.35 μm CMOS process was removed using a post-process silicon dioxide RIE. TMAH (tetra methyl ammonium hydroxide) is then used to remove the silicon substrate underneath the inductor to achieve a suspended spiral inductor. The advantage of the post processing is its compatibility with the CMOS process.

There are several works that have used identical techniques to improve the *Q* factor; however, they have applied different processes [26, 47, 48]. The main issue in these approaches is the restricted separation that can be obtained (only tens of μm or less). In addition, substrate etching must be carried out in a compatible process, but the concerns about the reduced mechanical stability of the substrate remain [7].

3.2.3 Patterned Grounded Shield

Another method to reduce the substrate effect is to use a patterned grounded layer between the spiral coil and the substrate in order to cause $R_{Si} \to 0$ and thus, $R_p \to \infty$. Hence, the substrate loss factor moves to the unity value. Using this method, an enhancement in the *Q* factor was achieved by employing patterned ground by [15]. The effect of using a patterned ground can also be clarified from the effects of increasing the effective area of the segments. However, this increases the parasitic capacitive coupling to ground [49].

3.2.4 Increase of Distance between the Substrate and the Coil (Suspended Inductor)

One of the effective parameters in the substrate loss factor is C_{ox}; this parameter can make the substrate loss factor close enough to unity while it itself limits to zero. By knowing the basic equation of capacitance, C = $\varepsilon A/d$, where ε, *A*, and *d* are the dielectric, area of windings, and distance between windings and the substrate, respectively, it can be observed that any increase in distance causes a decrease in capacitance. Figure 9 illustrates the quality factor of a spiral inductor with different windings-substrate distances. It simply shows that the substrate loss factor improves when the distance increases.

A suspended spiral inductor, shown in Figure 10, was fabricated with MEMS technology on a glass substrate by [11], in which the coil was sustained with T-shaped pillars.

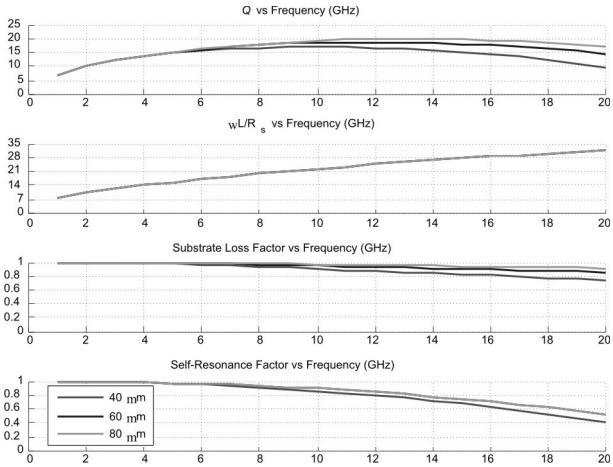

Figure 9: The calculated *Q* for different displacement distances

In the fabrication process, fine polishing of the photoresist was used to simplify the processes and ensure that the seed layer and the pillars made perfect contact. Dry etching techniques were employed to remove the seed layer. The inductor operates in a frequency range of 0.05–10 GHz, when the suspended height is 60 μm, the maximum *Q* factor is 37 for 4.2nH at 2 GHz. The result of this study is that the maximum quality factor grows gradually with an increase of the suspended height.

A substrate removal process using CMOS_MEMS can be found in [10]. In this work, a post-process was adopted to remove the silicon substrate under the manufactured spiral inductor in order to enhance the *Q*-factor of the inductor. This post-process utilizes CHF_3/O_2 RIE to etch the sacrificial layer of silicon dioxide, and then TMAH is used to remove the underlying silicon substrate. The suspended spiral inductor achieved a measured *Q*-factor of 15 at 11 GHz and a measured inductance of 4 nH at 25.5 GHz.

3.3 Self-Resonance Loss Factor

In the third term of equation (1), there are two main parameters C_s and C_p, which cause the self-resonance loss (SRL) factor to approach unity. In this case, the unity

SRL factor occurs when these two parameters are zero or near to zero.

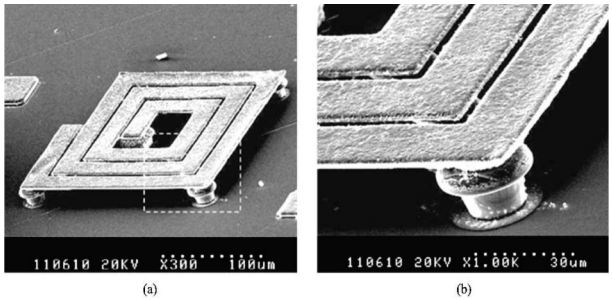

Figure 10: Suspended spiral inductor by [11]

The parasitic capacitance C_s is limited to zero when the spaces between the segments of the winding are not that close. In addition, C_p depends on C_{ox}, such that a zero-value C_{ox} leads to a zero-value C_p; the methods are very similar to the ones described for substrate loss factor when C_p approaches to zero, such as substrate removal and suspended spiral inductor.

4 Tunable MEMS inductor and methods to increase the tuning range

Tunable MEMS inductors will find their way to market by 2015 in reconfigurable mobile handsets, reconfigurable satellite communications and base stations, and 60 GHz WLAN applications [35]. A tunable MEMS inductor of a small size with high *Q* factor and ability of tuning is the required component in most wireless applications, such as reconfigurable LNAs, VCOs, and Filters.

In previous discussions, the quality factor of the inductor was discussed in detail. Here, a discussion around the tuning range will be presented. The tuning range parameter is the other important value for inductor design. There are some factors that affect the tuning range and are used as methods to enhance it. These methods are discussed in the following.

4.1 Change of the Number of Turns

Here, equation (10) is used as the reference equation for the inductance of the spiral inductor. From (10), the factors that can affect the inductance in order to control the inductance and hence, the tuning range, can be extracted. Inductance is directly proportional to the square of the number of the turns N^2. Therefore, controlling the number of turns can provide control of the inductance value. Some previous works used this property to tune the inductance by their own techniques. Figure 11 illustrates the inductance variation while the turns are switched.

$$M^{+} = \frac{\mu_0 L(N-1)}{4\pi} \times \ln\sqrt{1+\left(\frac{L}{4NS}\right)^2} + \frac{L}{4NS} - \sqrt{1+\left(\frac{4NS}{L}\right)^2} + \frac{4NS}{L} \quad (13)$$

$$M^{-} = \frac{\mu_0 LN}{4\pi \times 214} \quad (14)$$

4.1.1 Switched Turns of Inductor

In this method, inserting switches (or relays) between the turns of the inductor causes it to bypass a specific number of turns and hence, change the inductance. The structure of such an inductor is shown in Figure 12(*a*) [25].

This method was improved by using MEMS switches instead of the micro-relays in [9]. The model of the fabricated tunable MEMS inductor can be found in Figure 12(*b*). Here, an RF MEMS switch was employed to bypass a determined number of turns. The proposed tunable inductor was used to reconfigure the bandwidth of Bulk Acoustic Wave (BAW) ladder filters. From the simulation, it was realized that use of this method increases the filter bandwidth by 25%.

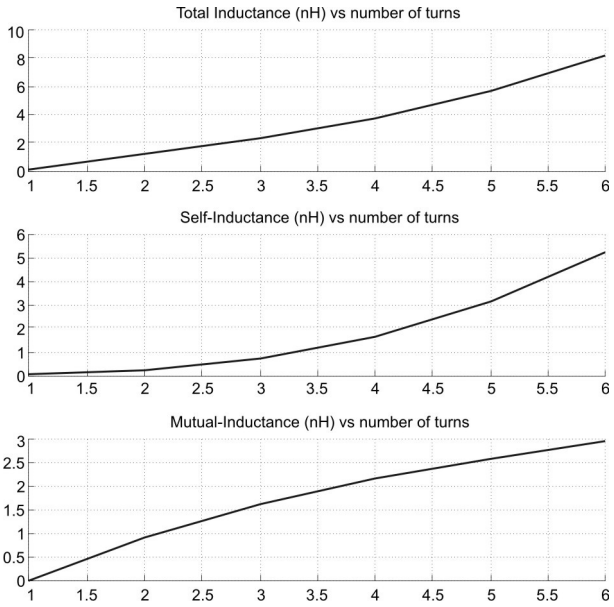

Figure 11: Inductance variation versus number of turns

The measurement results showed an inductance of 4 nH when the first switch was activated and an inductance of 1 nH when the second switch was activated at a frequency of 3 GHz. The switches gave a sufficient operation for a frequency range of 1–5 GHz.

4.1.2 Use of Conductive Liquid

One of the novel methods for tunable inductor implementation is to use conductive material in order to by-

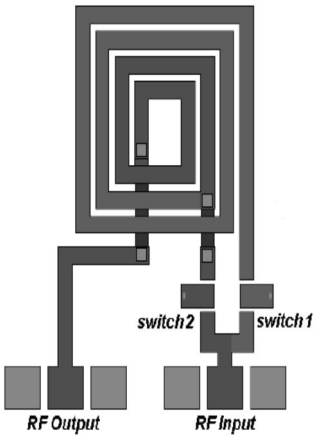

(a)

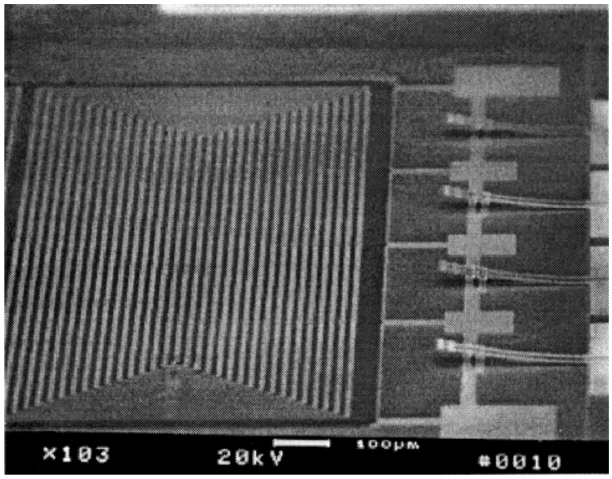

(b)

Figure 12: *(*a) A switched-turn variable inductor by [25], (b) A MEMS switched-turn variable inductor by [9]

pass the specific number of the turns. This method can be found in [20], in which the variable inductor contains a planar spiral inductor, a micro pump, and conductive liquid metal (Mercury), and all of these were implemented in one single chip. According to the direct proportionality between the inductance and the square of the number of turns, using voltage electrodes makes the mercury move between the spaces of the intercoil, such that part of intercoil becomes short-circuited. This phenomenon results in a reduction of stored magnetic energy and indeed, the inductance. The tuning range in this work is above 100% at 8 GHz (see Figure 13).

4.2 Change of Coupling Capacitance

4.2.1 Change of Dielectric Value (Cross-Talk Strength)

Another novel method was introduced by [20] in which the capacitive coupling between the inter-spires is varied by a reduction of the stored magnetic energy; this occurs when liquid moves between the metal spires.

The liquids that can be employed in this method are divided in two categories: liquid metals and ionic liquids. Liquid metals have conductivity a thousand times higher than ionic liquids, but ionic liquids are much easier to handle. Mercury is the most famous and most often used liquid metal in previous works, but it is toxic and harmful to the environment.

In [22, 23], this method was implemented with various liquids. A very high tuning range of up to 107% was achieved by employing salted water at 1.6 GHz frequency with a *Q* factor of 12. The structure of this variable inductor is shown in Figure 14.

The effect of salts on water permeability varies depending on the salts and the species (Figure 15). While most salts, such as: KCl, KNO_3, $(NH_4)_2SO_4$, $NaNO_3$, NaCl, NH_4Cl, $AlCl_3$, and NH_4NO_3) had no pronounced effect, $CaCl_2$, K_2CO_3, and Cs_2CO_3 were very efficient in increasing cuticular water permeability's of *H. helix, P. laurocerasus*, and *L. esculentum* (Figure 16). The effects of $CaCl_2$ were 2.41 ± 0.26, 1.29 ± 0.11, and 1.55 ± 0.31 for the three measures. The effects of K_2CO_3 were 1.43 ± 33, 1.68 ± 0.13, and 2.63 ± 0.28, and the effects of Cs_2CO_3 were 1.52 ± 0.18, 2.60 ± 0.29, and 2.50 ± 0.48 [50].

Figure 16 presents the simulation for a liquid tunable inductor using salted water. The salted water is injected in a tunable liquid inductor, such as in Figure 14.

As the liquid moves in the turns of the inductor, the total inductance, including the self-inductance and mutual inductance, changes. In Figure 16, the top plot shows the variation of the total inductance when the water is injected in turns 1 to 6.

The middle plot shows the self-inductance for the turns that salted water is injected and the turns in which air still remains. The bottom plot shows the mutual inductance variation when more salted water is injected.

4.2.2 Changing Coupling between the Substrate and the Coil

When the coil is implemented on a low-resistivity substrate, the planar inductor geometries present both a desired inductance and a parasitic capacitance. A reduction in the size of the winding metals leads to a reduction in parasitic capacitance, but in addition, to an increase in the resistive loss. This method is useful for improving the tuning range and also the *Q* factor, and is based on the coil structure displacement away from the substrate. This causes a reduction in capacitance between the coil and the substrate while the resistance remains constant.

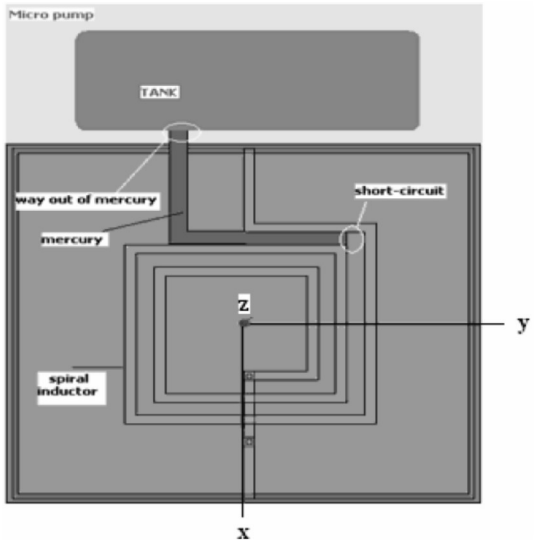

Figure 13: Conductive liquid inductor by [20]

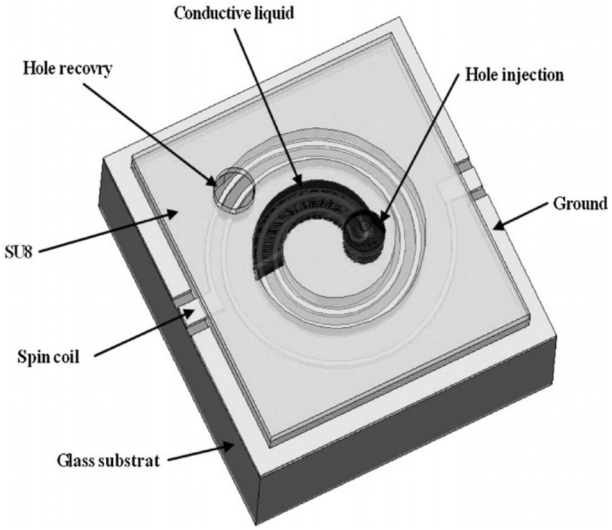

Figure 14: Liquid variable inductor with salted water [22, 23]

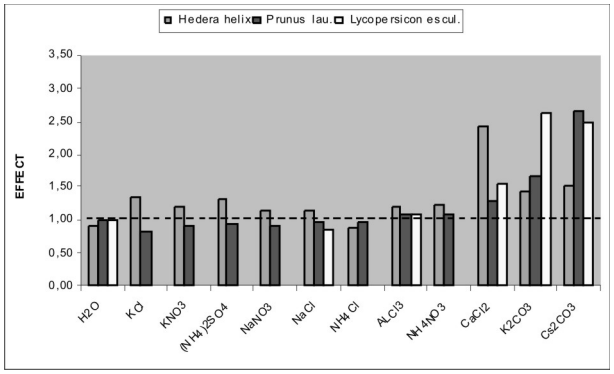

Figure 15: Effects of different salts on water permeability [50]

In [24], a MEMS tunable inductor was assembled using an interlayer stress, such that it causes portions of the inductor to bend away from the substrate in a controlled manner. This is allowed by fabricating the inductor in the substrate plane over a sacrificial layer with anchor points at both ends connecting through to the substrate.

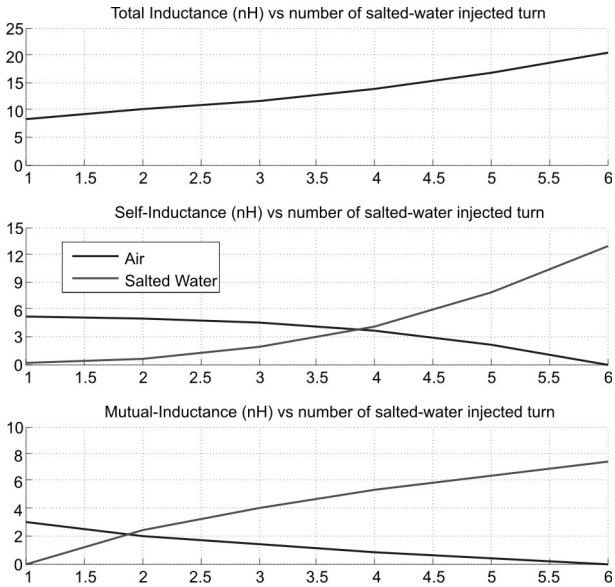

Figure 16: Inductance variation versus number of turns with injected salted water

Employing two or more deposited material layers with dissimilar stresses, the inductor can be forced to curl away from the substrate while the sacrificial layer is removed.

Following the same method, an spiral inductor was fabricated by [21]. A tunable inductor was achieved based on the structure shown in Figure 17. In this work, the tunable MEMS inductor, based on the bimorph effect, was fabricated with amorphous silicon (a-Si) and aluminum structure layer on a-Si and c-Si substrates at low temperature (150 °C). Because of interlayer stress between the two layers (films), the coil warps. This stress is controllable by film thickness and hydrogen content. When a voltage is applied between the terminals, due to the difference in thermal expansion coefficient (TEC) of the two materials, the structure deforms in a controllable manner. A tuning range of 32% (5.6–8.2 nH) was achieved at a frequency of 4 GHz with a *Q* factor of 15 and resonance frequency of 7 GHz.

4.3 Change of the Mutual Inductance (Coupling Coefficient) between Two Coils

By controlling the magnetic coupling coefficient between two different inductors, a tunable inductor is

achieved. Usually, for two identical inductance L_0, the mutual inductance *M*, can be achieved by [51, 52]:

$$M = L_0 \quad K \tag{15}$$

where the coupling factor is given by *K*. No matter if the inductors are connected in parallel or series, when the current flows in two adjacent lines, the same or opposite direction will happen.

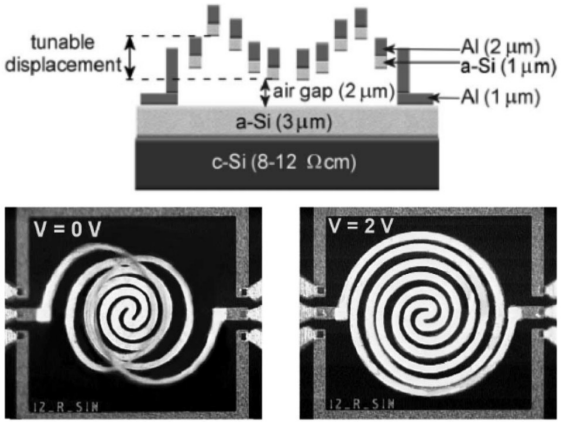

Figure 17: Tunable MEMS inductor based on bimorph effect by [21]

For the same direction, M is positive and for opposite, M is negative. In theory, the value of *K* is between 0 and 1.

In this method, two or several parallel inductors are fabricated, one of which is in flow and the other are switched off or moved away with different actuators. The motion/switching of one inductor changes the mutual inductance between that inductor and the fixed inductor by changing the coupling factor between two coils. This results in a change in the overall inductance by $L = M / K$. Figure 18 shows work by [5] that uses switched inductors to control the mutual inductance and hence, the overall inductance. When all the micromechanical vertical switches are open, the inductance seen from port one is L_1. Inductors at port two are different in size and thus, have a different mutual inductance effect on port one when activated. The number of different possible states *P* of the inductance can be achieved by:

$$P = 1 + n(n+1)/2 \tag{16}$$

where n represents the number of the inductors at port two.

Equivalent inductance and series resistance, seen from port one, can be achieved as follows [5]:

$$L_{eq} = \left(L_1 - \sum_{i=2}^{n+1} \frac{b_i K_i^2 L_i^2 \omega^2}{R_i^2 + L_i^2 \omega^2} \right) \tag{17}$$

$$R_{eq} = \left(R_1 - \sum_{i=2}^{n+1} \frac{b_i R_i K_i^2 L_1 L_i^2 \omega^2}{R_i^2 + L_i^2 \omega^2} \right) \tag{18}$$

where $b_i = 0$ or 1, L_i gives the inductance value of the secondary inductors, R_i denotes the series resistance of each secondary inductor in addition to the contact resistance of its corresponding switch, k_i represents the coupling coefficient, b_i is the state of the switch with a value of 1 or 0 depending on whether the switch is on or off, respectively, and ω gives the angular frequency. The maximum effective inductance happens when all the switches at port two are on. Here, the tuning range can be achieved from [5]:

$$\%tuning = \sum_{i=2}^{n+1} \frac{b_i K_i^2 L_i^2 \omega}{R_i^2 + L_i^2 \omega^2} \times 100 \tag{19}$$

using this method with two inductors at port two, the maximum tuning range of 47% was achieved at 6 GHz for a 1.1 nH silver inductor [5].

Using equation L_{eq}, the variation of inductance when four inductors on port two are switched into the circuit, is plotted in Figure 19. The x-axis shows the state of the switches for inductors L_2 to L_5, which are sorted by descending inductance values. The maximum inductance happens when no inductor is switched ('0000'), which is equal to L_1. When all inductors are switched into the circuit ('1111'), the minimum inductance occurs. Theoretically, it can be seen that by switching inductors, a linear variation of inductance can be achieved to some extent. In this simulation, a tuning range of 98% was achieved with four switched inductors, while a value of 68% for the tuning range can be achieved for two switched inductors. This is a value close to the tuning range achieved by measurement in [5]. Using the mutual inductance adjusting method, a tunable inductor was proposed by [53, 54]. In this work, a MUMPS process was employed, which is used for thin metal layers deposited on polysilicon. The main idea in this work is the displacement of the moving inductor away from the substrate.

Two inductors in parallel were fabricated, in which the inner inductor is fixed on chip and the outer inductor is moving off the substrate by outstanding stress between the metal and the polysilicon layer. The outer inductor is attached to a beam that is connected to an array of thermal actuators. By actuating the array, the beam bends and the outer inductor is lifted up. The mutual inductance and hence, the total inductance are

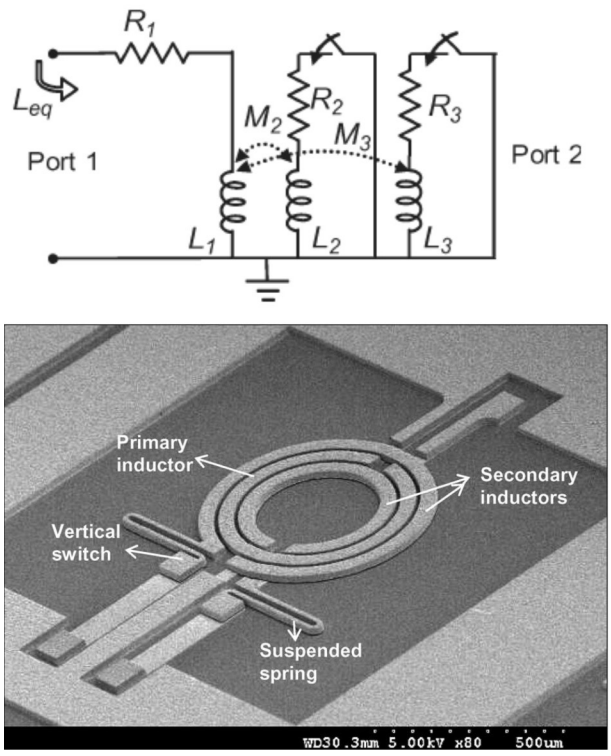

Figure 18: Tunable inductor using mutual inductances activated by micromechanical switches to achieve four discrete values [5].

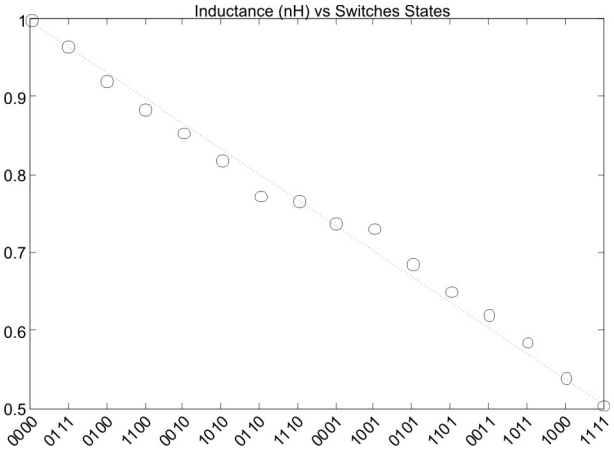

Figure 19: Inductance variation versus different states of mutual-controlled inductor with four peripheral coils

tuned by the control of the angle that separates the two inductors.

Using the same method, a tuning range of 30% was achieved by [55] at a frequency of 7 GHz with a resonance frequency of 35 GHz. The maximum *Q* factor was 25. A CMOS-compatible process was used for the fabrication of this inductor. This inductor also works with thermal bimorph structures; however, it can be replaced with electrostatic or piezoelectric actuators.

Using an identical technique, a tunable inductor was implemented by [27]. In this work, the inductance is controlled by the primary coil. The secondary short-circuited coil is magnetically coupled to the primary one. The magnetic flux relation between the coils induces eddy currents in the secondary coil. By changing the magnetic coupling between the inductors, the equivalent inductance seen at the primary port is changed (see Figure 20).

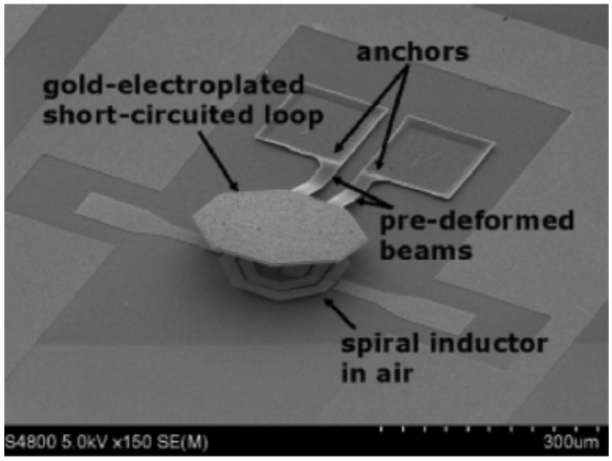

Figure 20: Mutual-controlled variable inductor with magnetic flux control of the secondary coil by [27]

4.4 Change of the Magnetic Flux

4.4.1 Change of the Permeability

Changing the permeability of the core is another approach to implement a tunable inductor. This method has been used mostly for 3D solenoid inductors in previous works. In this type of inductor, the core material can be air, but also any ferromagnetic metal. With different core materials, different inductance values can be achieved. In addition, moving the core changes the magnetic field and hence, changes the inductance.

Using this property, several different types of tunable MEMS inductor were implemented. One of the earlier works was [31], in which an electrically tunable RF inductor, based on a planar solenoid with a thin-film ferromagnetic (FM) core (NiFe), was realized. Variation of inductance was achieved by employing an additional dc current through the same device and thus, altering the effective permeability of the FM core caused a shift in inductance. For inductance ranges of 1 to 150 nH, tuning ranges of 85%, 35%, and 20% were attained at 0.1, 1, and 2 GHz, respectively.

Figure 21 shows another work by [29, 30] in which a solenoid inductor with a Piezomagnetic core was fabricated. The central part of the PZT bridge extends or shortens depending on the sign of the DC voltage V

(typically from 1 to 10 volts) applied on each pair of sided-electrodes. This causes a transfer of uniaxial tensile or compressive planar stress σ_{uniax} to the ferromagnetic core, whose permeability μ_{dc} alters as a result of the magnetoelastic effect. The permeability and consequently, the inductance was controlled through the magnetoelastic field, denoted here as the H_p pressure field.

$$\propto_{dc}(V) = \frac{M_s}{H_{eff} + H_p(V)} \tag{20}$$

$$H_p(V) = \frac{3}{M_s}\lambda_s \times \sigma_{uniax}(V) \tag{21}$$

$$H_{eff} = H_K + H_d \tag{22}$$

where H_k and H_d are the induced uniaxial anisotropy, and the demagnetizing field determined by the composition of the material and by the geometry of the core, respectively. Based on the sign of σ_{uniax}, H_p can be positive or negative, having a high saturation magnetization M_s = 1.8 T and an intermediate positive saturation magnetostriction λ_s=20x10^{-6}.

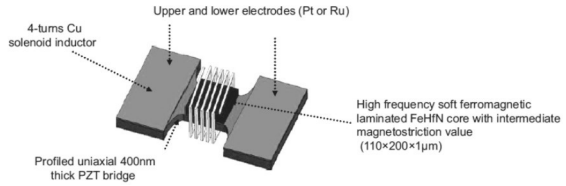

Figure 21: Solenoid inductor with permeability-controlled Piezomagnetic core [29, 30]

The following equation shows the relationship between the frequency and the permeability by using the general Landau-Lifshitz-Gilbert (LLG) equation achieved for thin film ferromagnetic film:

$$\mu(\omega) = 1 + \gamma M_s \left[\frac{\gamma H_{eff} + \gamma M_s + j\omega\alpha}{[\gamma H_{eff} + j\omega\alpha][\gamma M_s + j\omega\alpha] - \omega^2} \right] \tag{23}$$

where Ms gives the saturation magnetization and Heff is the total effect field, α is phenomenological damping constant, γ is the gyromagnetic ratio, and ω is the frequency of operation.

In the latest work, using the permeability property, a spiral planar inductor with a movable magnetic core of Ferrofluid, shown in Figure 22, was implemented by [28]. A variable planar inductor based on Ferrofluid actuation was reported. Here, the distribution of the permeability over the spiral inductor was adjusted by the movable Ferrofluid magnetic core. Ferrofluid in a reservoir created on the inductor is displaced using magnetic field gradients produced by another planar coil (actuation coil) aligned to the inductor. A bias field is used to enable repelling of the fluid from the inductor. The tuning range is 16% at 320 MHz and a maximum quality factor is 23 at 60 MHz.

4.4.2 Counteractive Magnetic Field Induction

In this technique, variable inductance is achieved by moving a metal plate on top of the coil. A MEMS actuator is usually used to move this plate. The controlled shielding of the magnetic flux varies the inductance. The parallel-plate actuator forms a capacitor and thus, current does not flow between the electrodes. A counteractive magnetic field according to Lenz's law is induced by entering the magnetic flux of the spiral inductor into the metal plate and introducing eddy currents.

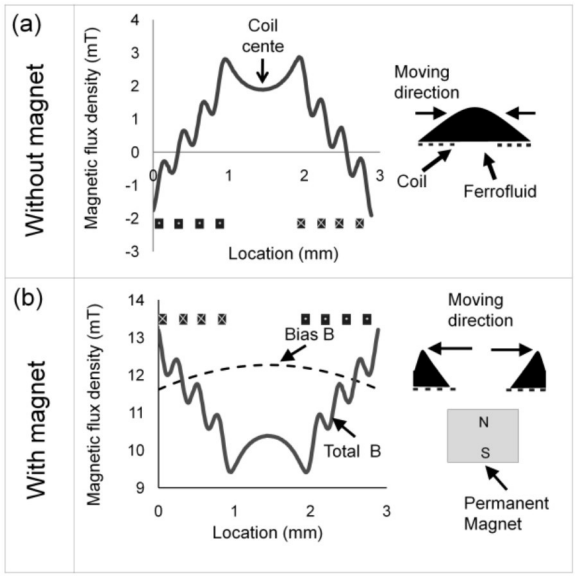

Figure 22: Variable planar inductor with movable Ferrofluid magnetic core [28].

The magnetic flux is shielded by the metal plate. This causes the metal plate's height h to decrease and inductance varies according to *h* [33].

An on-chip high-*Q* variable spiral inductor embedded in a wafer-level chip-scale package (WL-CSP) was proposed by [32] with a MEMS-actuated moving metal plate. At 2 GHz, the measured inductance varies from 4.80 to 2.27 nH, i.e., the variable ratio is 52.6%. The maximum value of the quality factor is 50.1. Figure 23 shows this inductor modeled in Sonnet EM simulator. The simulated inductance and quality factor for two different position of the shield are given in Figure 24.

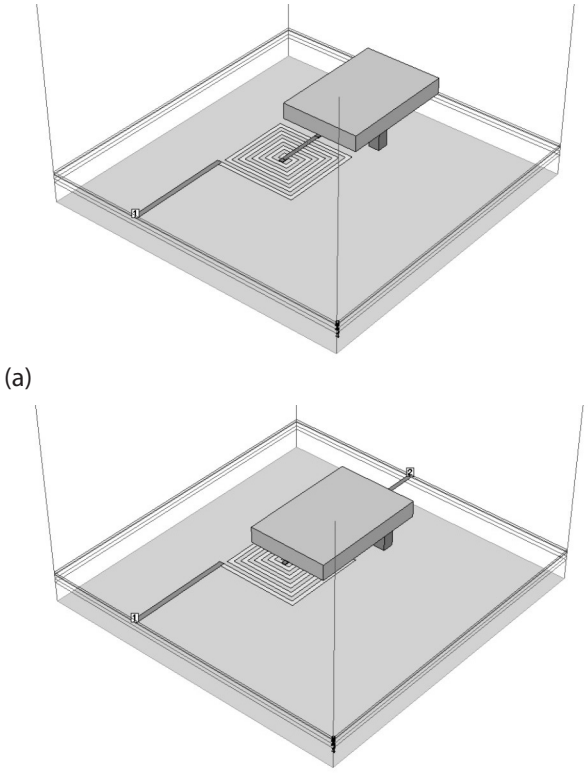

(a)

(b)

Figure 23: Variable inductance with controlled shielding of the magnetic flux: (*a*) not shielded, (*b*) half shielded in Sonnet.

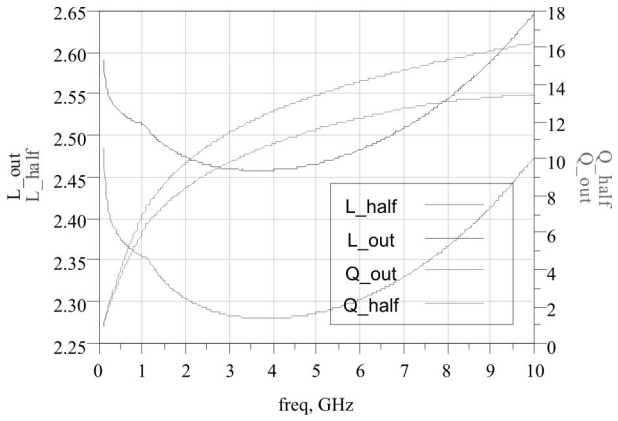

Figure 24: simulated inductance and quality factor for non-shielded (indexed with *out*), and half shielded (indexed with *half*)

5 Conclusion

This paper focused on exploration of the existing methods for the improvement of *Q* factor and tuning range of novel MEMS inductors. Based on the equations for *Q* and inductance values, these methods were categorized and various analyses were given in MATLAB and Sonnet to show their partial and overall performance. The achieved simulation results were close enough to the measurement results of inductors previously fabricated in earlier works, which were reviewed. Thus, the reader can choose the appropriate method based on the performance and complexity and then, study the equations and simulation results for any future enhancement.

6 Acknowledgment

Authors would like to thank Universiti Sains Malaysia research university (RU) grant No. 1001/PELECT/814168. Special acknowledgment to Universiti Sains Malaysia research university (RU) grant No. 1001/PELECT/814107 and Universiti Sains Malaysia ERGS grant No. 203/PELECT/6730112 for the funding of this work.

7 References

1. W. C. Tang and Y. L. Chow, "Inductance formula of a square spiral inductor on grounded substrate by duality and synthetic asymptote," 2002, pp. 2069-2072.
2. J. Zeng, A. Pang, C. Wang, and A. Sangster, "Flip chip assembled MEMS inductors," *Electronics Letters,* vol. 41, pp. 480-481, 2005.
3. I. Zine-El-Abidine, M. Okoniewski, and J. G. McRory, "A new class of tunable RF MEMS inductors," 2003, pp. 114-115.
4. I. Zine-El-Abidine, M. Okoniewski, and J. G. McRory, "RF MEMs tunable inductor using bimorph microactuators," 2005, pp. 436-437.
5. M. Rais-Zadeh, P. A. Kohl, and F. Ayazi, "MEMS switched tunable inductors," *Microelectromechanical Systems, Journal of,* vol. 17, pp. 78-84, 2008.
6. S. Pinel, F. Cros, S. Nuttinck, S. W. Yoon, M. Allen, and J. Laskar, "Very high-Q inductors using RF-MEMS technology for System-On-Package wireless communication integrated module," 2003, pp. 1497-1500 vol. 3.
7. G. W. Dahlmann, E. M. Yeatman, P. R. Young, I. D. Robertson, and S. Lucyszyn, "MEMS high Q microwave inductors using solder surface tension self-assembly," 2001, pp. 329-332 vol. 1.
8. Y. C. Huang, B. H. Jang, and W. Fang, "Implementation and characterization of a quality-factor-controllable micromachined inductor," 2011, pp. 1168-1171.
9. S. Aliouane, A. Kouki, and R. Aigner, "RF-MEMS switchable inductors for tunable bandwidth BAW filters," 2010, pp. 1-6.
10. C. L. Dai, J. Y. Hong, and M. C. Liu, "High Q-factor CMOS-MEMS inductor," 2008, pp. 138-141.

11. X. N. Wang, X. L. Zhao, Y. Zhou, X. H. Dai, and B. C. Cai, "Fabrication and performance of a novel suspended RF spiral inductor," *Electron Devices, IEEE Transactions on,* vol. 51, pp. 814-816, 2004.
12. G. W. Dahlmann, E. M. Yeatman, P. R. Young, I. D. Robertson, and S. Lucyszyn, "MEMS high Q microwave inductors using solder surface tension self-assembly," in *Microwave Symposium Digest, 2001 IEEE MTT-S International*, 2001, pp. 329-332 vol.1.
13. J. Chen, J. Zou, C. Liu, J. E. Schutt-Ainé, and S. M. K. Kang, "Design and modeling of a micromachined high-Q tunable capacitor with large tuning range and a vertical planar spiral inductor," *Electron Devices, IEEE Transactions on,* vol. 50, pp. 730-739, 2003.
14. W. Dae-Hee, J. Jong-Hyeok, K. Jeong-Il, S. Mohammadi, and L. P. B. Katehi, "High-Q integrated 3-D inductors and transformers for high frequency applications," in *Microwave Symposium Digest, 2004 IEEE MTT-S International*, 2004, pp. 877-880 Vol.2.
15. C. P. Yue and S. S. Wong, "On-chip spiral inductors with patterned ground shields for Si-based RF ICs," *Solid-State Circuits, IEEE Journal of,* vol. 33, pp. 743-752, 1998.
16. D. H. Weon, J. I. Kim, and S. Mohammadi, "Design of high-Q 3-D integrated inductors for high frequency applications," *Analog Integrated Circuits and Signal Processing,* vol. 50, pp. 89-93, 2007.
17. C. Leroy, M. B. Pisani, C. Hibert, D. Bouvet, M. Puech, and A. M. Ionescu, "High quality factor copper inductors integrated in deep dry-etched quartz substrates," *Microsystem technologies,* vol. 13, pp. 1483-1487, 2007.
18. P. J. Chen, W. C. Kuo, W. Li, Y. J. Yang, and Y. C. Tai, "Q-enhanced fold-and-bond MEMS inductors," 2008, pp. 869-872.
19. D. H. Weon, J. I. Kim, J. H. Jeon, S. Mohammadi, and L. P. B. Katehi, "High performance micro-machined inductors on CMOS substrate," 2005, p. 4 pp.
20. I. Gmati, H. Boussetta, M. A. Kallala, and K. Besbes, "Wide-range RF MEMS variable inductor using micro pump actuator," 2008, pp. 1-4.
21. S. Chang and S. Sivoththaman, "A tunable RF MEMS inductor on silicon incorporating an amorphous silicon bimorph in a low-temperature process," *Electron Device Letters, IEEE,* vol. 27, pp. 905-907, 2006.
22. I. El Gmati, P. F. Calmon, A. Boukabache, P. Pons, R. Fulcrand, S. Pinon, H. Boussetta, M. A. Kallala, and K. Besbes, "Fabrication and evaluation of an on-chip liquid micro-variable inductor," *Journal of micromechanics and microengineering,* vol. 21, p. 025018, 2011.
23. I. El Gmati, P. Calmon, A. Boukabache, P. Pons, H. Boussetta, M. Kallala, and K. Besbes, "Liquid RF MEMS variable inductor," *Procedia Engineering,* vol. 5, pp. 1380-1383, 2010.
24. V. M. Lubecke, B. Barber, E. Chan, D. Lopez, M. E. Gross, and P. Gammel, "Self-assembling MEMS variable and fixed RF inductors," *Microwave Theory and Techniques, IEEE Transactions on,* vol. 49, pp. 2093-2098, 2001.
25. S. Zhou, X. Q. Sun, and W. N. Carr, "A monolithic variable inductor network using microrelays with combined thermal and electrostatic actuation," *Journal of micromechanics and microengineering,* vol. 9, p. 45, 1999.
26. I. Zine-El-Abidine, M. Okoniewski, and J. McRory, "A MEMS tunable inductor," pp. 340-2.
27. J. I. Kim and D. Peroulis, "Tunable MEMS spiral inductors with optimized RF performance and integrated large-displacement electrothermal actuators," *Microwave Theory and Techniques, IEEE Transactions on,* vol. 57, pp. 2276-2283, 2009.
28. B. Assadsangabi, M. S. M. Ali, and K. Takahata, "Ferrofluid-based variable inductor," in *Micro Electro Mechanical Systems (MEMS), 2012 IEEE 25th International Conference on*, 2012, pp. 1121-1124.
29. O. Casha, I. Grech, J. Micallef, E. Gatt, D. Morche, B. Viala, J. P. Michel, P. Vincent, and E. de Foucauld, "Utilization of MEMS tunable inductors in the design of RF voltage-controlled oscillators," 2008, pp. 718-721.
30. M. El Bakkali, F. Chan Wai Po, E. De Foucauld, B. Viala, and J. P. Michel, "Design of a RF matching network based on a new tunable inductor concept," *Microelectronics journal,* vol. 42, pp. 233-238, 2011.
31. M. Vroubel, Y. Zhuang, B. Rejaei, and J. N. Burghartz, "Integrated tunable magnetic RF inductor," *Electron Device Letters, IEEE,* vol. 25, pp. 787-789, 2004.
32. K. Okada, H. Sugawara, H. Ito, K. Itoi, M. Sato, H. Abe, T. Ito, and K. Masu, "On-Chip High-$ Q $ Variable Inductor Using Wafer-Level Chip-Scale Package Technology," *Electron Devices, IEEE Transactions on,* vol. 53, pp. 2401-2406, 2006.
33. H. Sugawara, Y. Yoshihara, K. Okada, and K. Masu, "Reconfigurable CMOS LNA for software defined radio using variable inductor," in *Wireless Technology, 2005. The European Conference on*, 2005, pp. 547-550.
34. S. S. Mohan, M. del Mar Hershenson, S. P. Boyd, and T. H. Lee, "Simple accurate expressions for planar spiral inductances," *Solid-State Circuits, IEEE Journal of,* vol. 34, pp. 1419-1424, 1999.
35. S. Lucyszyn, *Advanced RF Mems*: Cambridge Univ Pr, 2010.

36. M. Gabriel and R. Rebeiz, "RF MEMS Theory, design and technology," *Hoboken: John Wiely and Sons,* 2003.
37. J. Zhao, "A new calculation for designing multilayer planar spiral inductors," *EDN (Electrical Design News),* vol. 55, p. 37, 2010.
38. J. Lee, S. Park, H. C. Kim, and K. Chun, "Substrates and dimension dependence of MEMS inductors," *Journal of micromechanics and microengineering,* vol. 19, p. 085014, 2009.
39. J. J. Liou, "On-chip spiral inductors for RF applications: an overview," *JOUNAL OF SEMICONDUCTOR THCHNOLOGY AND SCIENCE,* vol. 4, pp. 149-167, 2004.
40. W. B. Kuhn and N. M. Ibrahim, "Analysis of current crowding effects in multiturn spiral inductors," *Microwave Theory and Techniques, IEEE Transactions on,* vol. 49, pp. 31-38, 2001.
41. O. Ban-Leong, X. Dao-Xian, K. Pang-Shyan, and L. Fu-jiang, "An improved prediction of series resistance in spiral inductor modeling with eddy-current effect," *Microwave Theory and Techniques, IEEE Transactions on,* vol. 50, pp. 2202-2206, 2002.
42. C. Jinghong, Z. Jun, L. Chang, J. E. Schutt-Aine, and S. M. K. Kang, "Design and modeling of a micromachined high-Q tunable capacitor with large tuning range and a vertical planar spiral inductor," *Electron Devices, IEEE Transactions on,* vol. 50, pp. 730-739, 2003.
43. X. N. Wang, X. L. Zhao, Y. Zhou, X. H. Dai, and B. C. Cai, "Fabrication and performance of novel RF spiral inductors on silicon," *Microelectronics journal,* vol. 36, pp. 737-740, 2005.
44. C. M. Nam and Y. S. Kwon, "High-performance planar inductor on thick oxidized porous silicon (OPS) substrate," *Microwave and Guided Wave Letters, IEEE,* vol. 7, pp. 236-238, 1997.
45. W. B. Kuhn, X. He, and M. Mojarradi, "Modeling spiral inductors in SOS processes," *Electron Devices, IEEE Transactions on,* vol. 51, pp. 677-683, 2004.
46. S. H. Tseng, Y. J. Hung, Y. Z. Juang, and M. S. C. Lu, "A 5.8-GHz VCO with CMOS-compatible MEMS inductors," *Sensors and Actuators A: Physical,* vol. 139, pp. 187-193, 2007.
47. H. Lakdawala, X. Zhu, H. Luo, S. Santhanam, L. R. Carley, and G. K. Fedder, "Micromachined high-Q inductors in a 0.18-μm copper interconnect low-k dielectric CMOS process," *Solid-State Circuits, IEEE Journal of,* vol. 37, pp. 394-403, 2002.
48. H. Lakdawala, X. Zhu, H. Luo, S. Santhanam, L. Carley, and G. Fedder, "Micromachined high-Q inductors in 0.18 μm Cu interconnect low-K CMOS," in *Custom Integrated Circuits, 2001, IEEE Conference on.*, 2001, pp. 579-582.
49. D. Athreya, V. Sundaram, M. Iyer, and R. Tummala, "Ultra high Q embedded inductors in highly miniaturized family of low loss organic substrates," in *Electronic Components and Technology Conference, 2008. ECTC 2008. 58th*, 2008, pp. 2073-2080.
50. S. A. Elshatshat, "Effects of inorganic salts on water permeability of isolated cuticular membranes," PhD Thesis, University of Bonn, 2004.
51. C. M. Tassetti, G. Lissorgues, and J. P. Gilles, "New tunable RF MEMS microinductors design," *Journal of micromechanics and microengineering,* vol. 14, p. S17, 2004.
52. C. Tassetti, G. Lissorgues, and J. Gilles, "Tunable RF MEMS microinductors for future communication systems," 2003, pp. 541-545 vol. 1.
53. I. Zine-El-Abidine, M. Okoniewski, and J. G. McRory, "RF MEMS tunable inductor," 2004, pp. 817-819 Vol. 3.
54. I. Zine-El-Abidine, M. Okoniewski, and J. McRory, "A Tunable RF MEMS Inductor," 2004, pp. 636-638.
55. I. Zine-El-Abidine, M. Okoniewski, and J. G. McRory, "Tunable radio frequency MEMS inductors with thermal bimorph actuators," *Journal of micromechanics and microengineering,* vol. 15, p. 2063, 2005.

Arrived: 03. 10. 2013
Accepted: 27. 01. 2014